Synergistic effect of CeO_2 nanoparticles and WO_3 nanowires in gas sensing applications

Shuja Bashir Malik[1], Karol V. Mejia-Centeno[2], Paulina R. Martínez-Alanis[2], Andreu Cabot[2,3], Frank Güell*[1,4], Fatima Ezahra Annanouch[1] and Eduard Llobet*[1]

[1] Universitat Rovira i Virgili, MINOS, Països Catalans 26, 43007 Tarragona, Catalunya, Spain.
[2] Catalonia Energy Research Institute – IREC, Jardins de les Dones de Negre 1, Sant Adrià de Besós, 08930, Barcelona, Catalunya, Spain.
[3] ICREA, Pg. Lluis Companys, 08010, Barcelona, Catalunya, Spain.
[4] ENFOCAT, Universitat de Barcelona, Martí i Franquès 1, 08028 Barcelona, Catalunya, Spain.
*Corresponding authors: eduard.llobet@urv,cat, frank.guell@ub.edu

Abstract

The search for a highly selective ethanol sensor is still an open challenge. Metal oxides still face selectivity issues when it comes to gas sensing especially in case of ethanol. Keeping this in sight, in this work we explore the sensing properties of WO_3 nanowires grown via the aerosol assisted chemical vapour deposition and decorated with CeO_2 nanoparticles by drop casting. The nanocomposites were characterized by X-ray diffraction, field emission scanning electron microscopy, energy dispersive X-ray, photoluminescence, Raman and X-ray photoelectron spectroscopies. Upon exposure to different gas analytes, the electrical characterization showed that sensors responded well to ethanol both under dry and humid conditions (RH= 50 %, 25ºC), though the response towards ethanol decreased in humid atmospheres. The long-term stability was studied, and a gas sensing mechanism is introduced and discussed.

Keywords: metal oxide nanowires, gas sensors, nanoparticle decoration, AACVD, WO_3, CeO_2

1. Introduction

Air pollution as a result of rapid population boom and industrialization is a leading contributor to heart and lung diseases and premature deaths[1]. NO_2 is one of the main air pollutants among others like sulphur dioxide (SO_2), and ozone (O_3). The prime sources of NO_2 being burning of fossil fuels in automobiles, and industries. Volcanic eruptions and lightening are the natural sources of NO_2. On the other hand, carbon monoxide (CO) is a highly toxic, odourless, tasteless, and colourless gas. CO is a

leading ecological pollutant in developing and developed nations[2]. Exposure to CO over extended periods leads to decreased oxygen-carrying capacity of blood as the affinity of the human blood to CO is 250 to 300 times higher than oxygen[3]. Moreover, the discharge of chemical contaminants from industries has received considerable attention as it is associated with the release of volatile organic compounds (VOCs)[4]. The presence of VOCs in our environment adversely effects human's health[5]. Even though ethanol is not among the most dangerous VOCs, it has received a wide attention for its multifarious applications. Ethanol is colourless and transparent at room temperature and pressure and highly volatile. It is widely used in the chemical industry, for example as a solvent in the synthesis of other organic chemicals or in paints, produced from agricultural products, ethanol is used as an additive to automotive gasoline, present in alcoholic beverages, food industry products and pharmaceuticals [6,7]. While ethanol consumption can lead to driving accidents, the exposure to ethanol vapours can lead, in the long term, to vomiting, eye irritation and drowsiness[8]. Furthermore, ethanol is also an inhibitor of central nervous system[9]. Additionally, ethanol vapours can form an explosive mixture in the air, thus making it potentially dangerous among other VOCs[4]. All these aspects make it mandatory for the development of sensitive and cost-effective ethanol sensors that can be widely used. Chemoresistive sensors, especially metal oxide gas sensors (MOS) have been reported for monitoring pollutant gases and VOCs[10]. MOS have been commercially available for over 60 years[11]. Owing to their robustness, cost-effectiveness, sensitivity and small size, MOS sensors are attractive for a wide range of applications[12]. However, it is difficult to apply a single MOS in practical applications as they need high operating temperatures and are poorly selective.

To overcome these challenges, heterojunctions of metal oxides have been explored as a way to improve sensing performance, particularly selectivity [13–15] The heterojunctions are found to be enhancing the sensor performance[16,17]. Noteworthily, a variety of methods have been devised to fabricate different heterojunctions to enhance the ethanol gas sensing properties of MOS for example, InO_2 nanoparticles (NPs) modified GaN composites have been reported for detecting nitrogen dioxide [18], CeO_2 modified WO_3 for detecting n-Butanol [19] or $ZnWO_4/WO_3$ composites for the trace detection of H_2S[20]. Zhang et al. [21] reported bimetal-organic framework (BMOF)-derived porous Co_3O_4-ZnO heterojunction

nanofibers. The sensors recorded a response of R_a/R_g of 101.5 at 275°C for 100 ppm of ethanol. Similarly, Li et al. [22] reported CeO_2-TiO_2 porous heterojunction nanosheets derived from BMOFs. The porous nanosheets exhibited response of 41.72 towards 50 ppm of ethanol at 25°C. On the other hand, Doan et al. [23] reported heterojunctions of n-ZnO/p-Co_3O_4. The sensors showed high response, outstanding selectivity, and good repeatability for low concentrations of ethanol (1 ppm) at 300°C. Fang et al. [24] used indium containing MOFs as sacrificial templates for preparing hollow structured metal oxides (In_2O_3 hollow microtubes). The In_2O_3 microtubes were decorated by the Pr-doped SnO_2 NPs. The heterojunctions showed a response of 75 towards 50 ppm ethanol at the optimum temperature, 240°C. Cao et al. [25] reported double-layer nanofilm by sputtering SnO_2 and co-sputtering SnO_2/$ZnSnO_3$ porous top layer with SnO_2 and ZnO targets. The sensors showed a response of 11.5 towards 50 ppm ethanol at 290°C. Wang et al. [26] reported ethanol gas sensors based on p-Bi_2O_3 and n-ZnO heterostructures. The sensors exhibited a response of 21.6 towards 100 ppm ethanol at 175°C. Moreover, the sensors were able to detect ethanol concentration ranging from 1 to 500 ppm. Li et al. [27] reported 3D SnO_2-ZnO aerogels by two step reactions and annealing process. UV irradiation in coordination with SnO_2-ZnO was used to detect very low concentration of ethanol, 10 ppb at 300°C.

N-type semiconducting metal oxides (ZnO, WO_3, SnO_2, CeO_2) show stable physicochemical properties and response towards targeted gases, thus have been investigated in gas sensing applications[28–30]. Owing to its wide band gap, CeO_2 films exhibit a large baseline resistance at room temperature, thus requiring high operating temperatures[31]. CeO_2 shows excellent stability and quick response and recovery times, which are essential for enhancing the gas-sensing behaviour of CeO_2-based nano and microstructures[32]. Making efficient heterostructures with an efficient surface/interface charge transport mechanism for achieving good gas-sensing qualities at low operating temperatures is the most challenging problem for developing novel CeO_2-based sensors. Moreover, CeO_2 exhibits the oxidation-reduction (Ce^{4+}/Ce^{3+}) capabilities making it one of the desired materials for gas sensors, photocatalysis and electrochemical sensors. Owing to its unique electronic structure and lower tendency to form a hydrogen bond with

interfacial water molecules, resulting in humidity independent gas sensing performances. Also, decorating WO_3 nanowires with CeO_2 significantly improves the ethanol sensing performance and excellent selectivity [33]. Employing CeO_2 nanoparticles with a size below 10 nm with WO_3 nanowires synergistically enhances the overall sensing performance of the sensors. Herein, WO_3 NWs were first synthesized via aerosol assisted chemical vapour deposition (AACVD) and then CeO_2 NPs were decorated onto the NWs by drop casting method. The sensing nanocomposites were characterized by field emission scanning electron microscopy (FESEM), X-ray diffraction (XRD), Raman spectroscopy, photoluminescence (PL) and X-ray photoelectron spectroscopy (XPS). The gas sensing properties of the pristine WO_3 NWs and CeO_2 decorated WO_3 NWs were analysed towards the detection of ethanol vapours under dry and humid conditions. To check their selectivity, sensors were exposed towards different analytes such as CO, NO_2, and H_2.

2. Experimental section

2.1. WO_3 NWs synthesis

Pristine WO_3 NWs were grown directly on a commercial alumina substrate consisting of a pair of screen-printed interdigitated Pt electrodes (with 300 µm electrode gap) on one side and a platinum resistive heater meander on the back side. In a typical synthesis procedure, 50 mg of tungsten hexacarbonyl $W(CO)_6$ (Sigma Aldrich) was dissolved in a solution of acetone (CAS: 67-64-1) and methanol (CAS: 67-56-1) (3:1). The solution was ultrasonicated to ensure full solubilization. The solution was placed in an ultrasonic bath to generate aerosol. N_2 gas with a flow of 0.5 L/min and 1 L/min was used as a carrier to transport the aerosol to the alumina substrate preheated to 400^{o}C in a hot wall reactor. Different gas flows are used to obtain different morphologies of WO_3 NWs. Randomly oriented WO_3 NWs with pointed tips are obtained with high carrier gas flow of 1 L/min. On the other hand, WO_3 NWs with floral tops are obtained with low carrier gas flow of 0.5 L/min. The growth process takes approximately 40 minutes. The chamber is left to cool down naturally. Keeping in view our previous studies with WO_3 nanowires of similar morphology [34–36], we decided to proceed with the morphology studied, because our previous results have shown that this one leads to better sensing

performance. The substrates with WO_3 NWs are annealed at 500ºC for 2 hours in a Carbolite CWF 1200 muffle furnace within a synthetic air environment. Annealing helps in removing any carbon residues from the solvents and results in fully oxidized WO_3 NWs.

2.2. CeO_2 NPs synthesis.

The CeO_2 NPs were synthetized according with the reported method by Berestok et al.[37]. In a 3-necked flask connected in a Schlenk line, 1 mmol of cerium (III) nitrate hexahydrate ($Ce(NO_3)_3{\cdot}6H_2O$, 99%, Sigma -Aldrich), 6 mmol of Oleylamine (OAm, 90%, Sigma -Aldrich) and 4 ml of 1-octadecene(ODE, 90% Sigma-Aldrich) were added. The reaction mixture was degassed at 80°C for 30 min with an argon flux. After degassing, the mixture was heated at 300 °C for one hour and then cooled to 160°C. Once at 160°C, 2 ml of toluene (analytical grade, Panreac) were added. The reaction mixture was dried under vacuum at 60°C. In order to eliminate the organic residues, the dried solid obtained was washed with 25 ml of acetone and subsequently centrifuged at 6500 rpm for 6 minutes. The solid was then washed three more times with 25 mL of chloroform followed by a final wash with acetone. All the washing steps were followed by a centrifugation step at 6500 rpm for six minutes. The final product was dried in vacuum for 40 minutes at room temperature. Finally, the product was placed in an oven under air flux with a ramp of 5ºC /min at 400°C for 4 hours.

2.3. CeO_2 NPs deposition on WO_3 NWs

The homogeneous suspension of 10 mg of CeO_2 NPs in 15 ml of chloroform was prepared by mixing in a 20 mL glass. 20 µl of the suspension was drop casted onto the WO_3 NWs substrates over a hot plate at 40ºC. Finally, the substrate was heated in an oven under air flux with a ramp of 5ºC /min at 400 °C for 4 hours.

2.4. Characterization techniques

The morphology of the WO_3 NWs decorated with CeO_2 NPs was examined using FESEM from Thermo Scientific Scios 2. Energy-dispersive X-ray (EDX) was performed in the same FESEM equipment. XRD measurements were made using a Bruker-AXS D8-Discover diffractometer equipped with

parallel incident beam (Göbel mirror), vertical θ-θ goniometer, XYZ motorized stage and with a GADDS (General Area Diffraction System). Samples were placed directly on the sample holder for reflection analysis. An X-ray collimator system allows to analyze areas of 500 μm. The X-ray diffractometer was operated at 40 kV and 40 mA to generate Cukα radiation. The GADDS detector was a VÅNTEC-500 (silicon strip technology) placed at 15cm from the sample. Three frames were collected (2D XRD pattern) that covered at such distance a range from 18 up to 80º 2θ. The exposition time was 300 s per frame. The resulting images were 2θ integrated to obtain a 2θ conventional diffractogram. The elemental and chemical composition was studied via XPS with a PHI 5500 Multitechnique System equipped with a monochromatic X-ray radiation source of Al Kα (1486.6 eV) at 350 W. The sample was placed perpendicular to the analyser axis and calibrated using the 3d5/2 line of Ag with a full width at half maximum (FWHM) of 0.8 eV. The diameter circle of the analysed area was 0.8 mm. The resolution for the general and depth profile spectra were 187.5 eV of pass energy at 0.8 eV/step, and 23.5 eV of pass energy at 0.1 eV/step, respectively. All measurements were made in an ultra-high vacuum (UHV) chamber with pressure (5·10-9 and 2·10-8 torr). The binding energies (BE) values are referred to the 1s BE at 284.8 eV. Component analysis has been performed by constructive curve joint Shirley and Tougaard functions to determine the peak background, and the line shape of the curves was fitted with mixed Lorentzian-Gaussian. The Raman spectroscopy measurements were obtained using a Renishaw laser 514 nm, ion argon-Novatech, 25 mW. The PL measurements at room temperature were made using a chopped Kimmon IK Series He-Cd laser (325 nm and 40 mW). Fluorescence was dispersed with an Oriel Corner Stone 1/8 74000 monochromator, detected using a Hamamatsu H8259-02 with a socket assembly E717-500 photomultiplier, and amplified through a Stanford Research Systems SR830 DSP. A filter of 360 nm was used against stray light. All spectra were corrected for the response function of the setups.

2.5. Gas sensing tests

The gas sensing characteristics of pristine and CeO_2 loaded WO_3 sensors were measured using a homemade detection system. Figure S1 (Supporting Information) shows the schematic of the

homemade measurement setup. The sensors were placed inside an inert, airtight Teflon® chamber (35 mL in volume) under a continuous gas flow of 100 sccm. The chamber can accommodate up to 4 sensors simultaneously. Calibrated gas bottles of hydrogen, ethanol, nitrogen dioxide and carbon monoxide balanced in dry air were employed. The carrier gas was zero-grade dry air. The gas analysis was set as pulses consisting of target gas concentrations with intercalated steps of dry air to recover to the baseline at a 100 ml min^{-1} constant flow. Reproducible concentrations of different gases were delivered into the chamber with the help of a computer-driven automated mass-flow control system. 5, 10, 15, and 20 ppm of ethanol, 1, 5, 7.5, 10, 15, and 20 ppm of carbon monoxide, 50 and 100 ppm of hydrogen and 100, 250, 500 and 1000 ppb of nitrogen dioxide concentrations were tested. After exposing the sensors to different gases, the baseline was recovered under dry air. The electrical resistance of the sensors was measured using an Agilent-34972A multimeter data acquisition system. The sensors were exposed to a particular analyte for 10 minutes and in order to recover the initial baseline, the chamber was purged with dry air for 60 minutes. The sensors were tested at various operating temperatures from 100^{o}C to 250^{o}C in intervals of 50^{o}C to understand the effect of the temperature on the sensor responses. The temperature coefficient of resistivity of the Pt heater printed in the backside of the alumina substrates is estimated using an oven and a multi-meter. These results are then used to set accurately the operating temperature of sensors. To analyse the effect of humidity and moisture cross-sensitivity on the sensing performance of the sensors, a liquid mass flow was employed for specific measurements in humidified backgrounds.

3. Results and discussion

3.1. Structural and morphological characteristics

Bare tungsten trioxide (WO_3) nanowires were successfully grown and directly integrated onto MEMS-based gas sensor substrates. Bare WO_3 nanowires were decorated with CeO_2 nanoparticles via drop casting technique. The colour of as deposited films was dark blue, which is an indication of having partially reduced tungsten oxide (WO_{3-x})[38], and also amorphous carbon from burnt organic solvents. The as-grown samples were annealed for 2 hours at 500°C in a muffle furnace under synthetic air. This annealing treatment at 500°C changes the thin film colour to pale yellow greenish, indicating the removal of most of the carbon impurities and that a nearly stoichiometric tungsten trioxide is achieved. Field emission scanning electron microscopy (FESEM) images give a good impression of the size and morphology of the CeO_2 decorated WO_3 nanostructures and are displayed in Figure 1. WO_3 nanowires with floral tops are obtained with low carrier gas flow of 0.5 L/min. The average diameter of the flowers is calculated as 798 nm. On the other hand, randomly oriented nanowires with pointed tips are obtained with high carrier gas flow of 1 L/min. The average length of the nanowires is higher than 1 µm. Nanowires show a tendency to grow vertically aligned to the substrate and are homogeneously dispersed across the entire electrode area of the commercial alumina substrates. Owing to the low loading of the CeO_2 nanoparticles, the CeO_2 nanoparticles were not seen in FESEM. However, EDX analysis of the thin films reveals the presence of CeO_2 decorations, (see Figure S2(b and c), Supporting Information). Peaks attributed to Al in the EDX diffractogram comes from the commercial alumina substrate Figure S2 (c). More details about the morphology of nanowires are given in the Supporting Information (in Table S1 and TEM details of CeO_2 nanoparticles are illustrated in Figure S3).

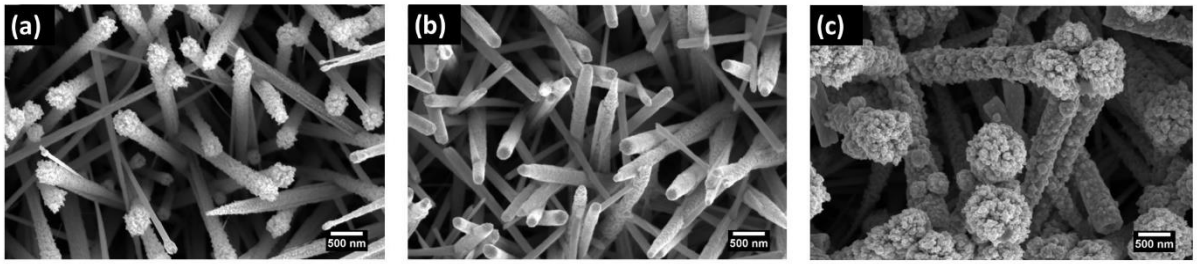

Figure 1: FESEM images (a) pristine WO_3 nanowires, (b) CeO_2 decorated WO_3 nanowires, and (c) CeO_2 decorated WO_3 floral tops nanowires.

The nanowires were analysed by XRD to investigate the crystallographic structures of pure and CeO_2 decorated WO_3 as depicted in Figure 2. The diffraction patterns of WO_3 in all the samples were indexed to ICDD card number 83-0951. It can be concluded from characteristic peaks that WO_3 has a monoclinic crystal structure and matches the space group of P21/n with lattice parameters, a= 7.301 Å, b= 7.538 Å, and c= 7.689 Å. WO_3 shows an intense diffraction peak at $2\theta = 24.36^{o}$ with preferred orientation in the (200) direction. The two types of WO_3 nanowires synthesized are single crystalline. The diffraction patterns of CeO_2 were indexed to ICDD card number 89-8436. From the diffraction pattern of CeO_2, it can be concluded that CeO_2 has a cubic crystal structure matching the space group Fm-3m with the lattice parameters a= 5.41120 Å. At 2θ=28.54, the peaks of WO_3 and CeO_2 almost coincide, hence in Figure 2 (b) and (c), the peak is intense than Figure 2 (a), pristine WO_3.

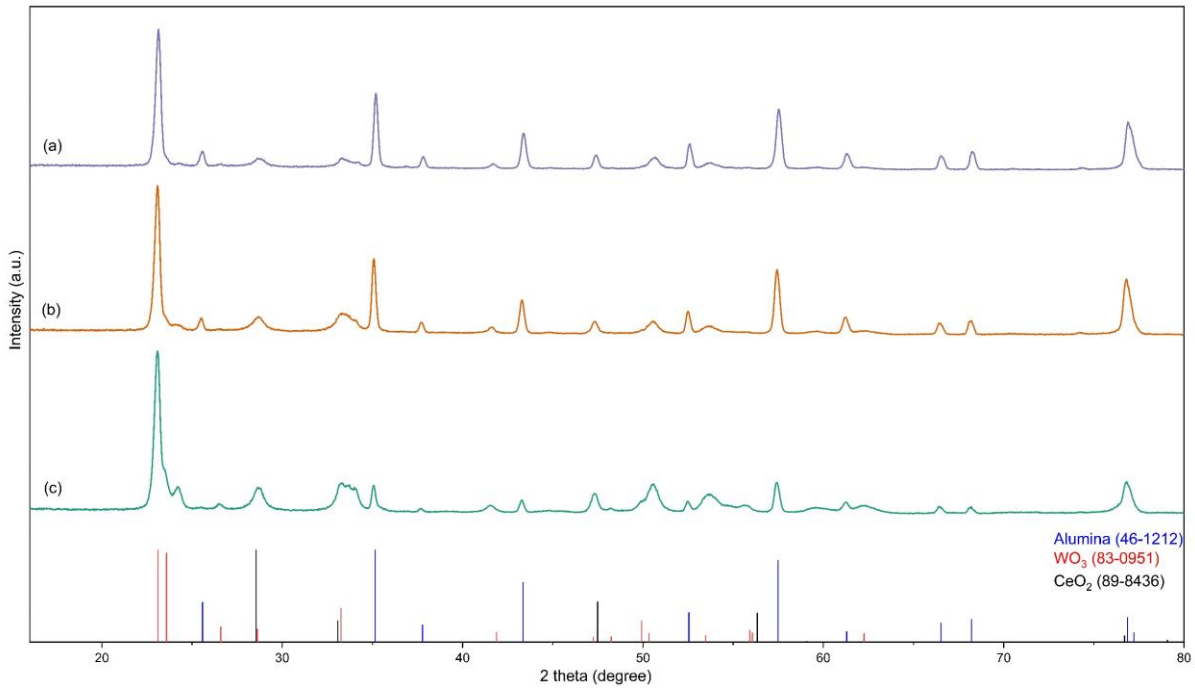

Figure 2: XRD diffractograms recorded of (a) WO_3, (b) CeO_2 decorated WO_3 randomly oriented and (c) CeO_2 decorated WO_3 with floral tops.

The PL spectra measured at room temperature are presented in Figure 3. The intensity of each spectrum was normalized to the maximum emission intensity for relative comparison. By pumping at 325 nm,

we observed an emission peak of the WO_3 nanowires at around 450 nm (2.75 eV) with a FWHM of 370 meV. When decorating the WO_3 nanowires with the CeO_2 NPs, the emission peak is shifted to 490 nm (2.53 eV) and 530 nm (2.34 eV) and the FWHM are around 1150 and 950 meV, respectively. This broadening observed on the FWHM indicates that the quantity of intrinsic defects is higher when decorating the WO_3 nanowires with the CeO_2 nanoparticles [39].

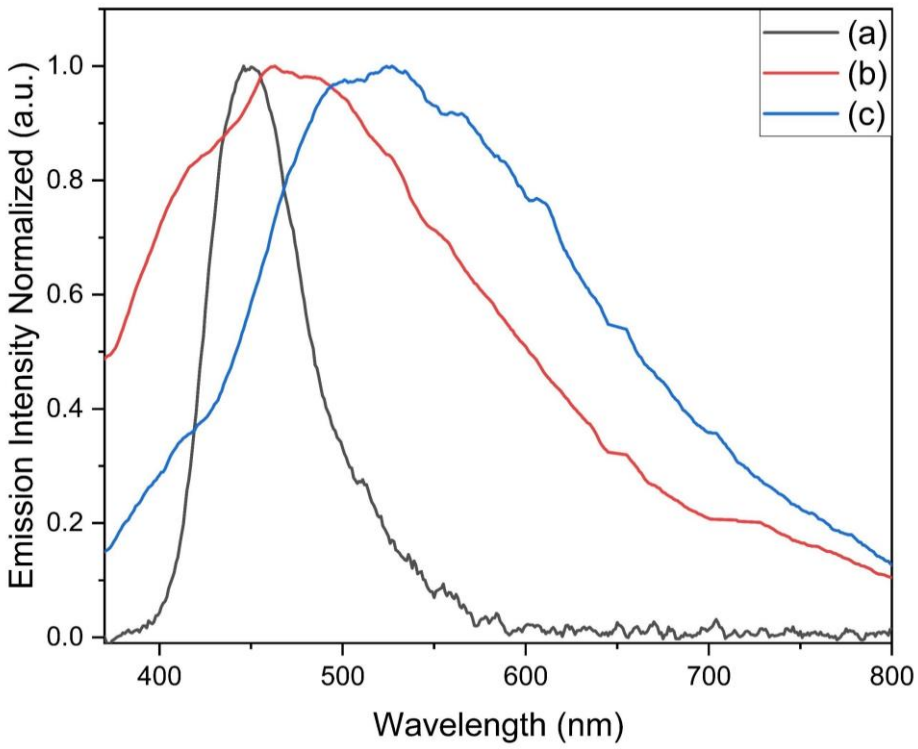

Figure 3: PL spectra of (a) WO_3, (b) CeO_2 decorated WO_3 randomly oriented nanowires, and (c) CeO_2 decorated WO_3 nanowires with floral tops.

Figure 4 shows the survey XPS spectra of the CeO_2/WO_3 NWs and CeO_2/WO_3 floral tops NWs. The analysis by XPS of the samples were performed using internal charge reference to C 1s at binding energy (BE) of 284.8 eV. Besides the C 1s peak corresponding to adventitious carbon, a low intensity peak at BE of 287-290 eV region was assigned to the presence of carbonate species. These carbonate species could be formed from CO_2 when the samples are exposed to ambient conditions. Figure 4(b) shows the spectra corresponding to the O1*s* core level, which can be deconvoluted into two components. The main contribution is by the band centred at around 530.3 eV BE, which could be related to lattice

oxygen (O_L). The broad band centred at around 531.9 eV binding energy indicates the presence of hydroxyl groups (OH). Hydroxyl contribution in the CeO_2/WO_3 NWs sample is higher than in the CeO_2/WO_3 floral tops NWs sample. The W4f BE shows two main peaks assigned to W^{6+} at 35.9 and 38.2 eV corresponding to $W4f_{7/2}$ and $W4f_{5/2}$, respectively. There are two minority peaks assigned to W^{5+} species at 34.9 and 36.5 eV corresponding to $W4f_{7/2}$ and $W4f_{5/2}$, respectively. The Ce 3d BE shows a complicated spectrum due the mixture of $Ce3d_{5/2}$ and $Ce3d_{3/2}$ species at 882.3 eV and 900.7 eV in the samples and their satellites. As per the spectra, the atomic concentration of the exposed Ce is increased, and the W atoms reduced in CeO_2/WO_3 NWs sample (Ce 15%, W 55%, O 37%) with respect to the CeO_2/WO_3 floral tops NWs sample (Ce 8%, W 48%, O 37%). These results suggest that CeO_2/WO_3 ratio could be responsible for the different sensing behaviour of the samples. The XPS results are in line with the XRD results.

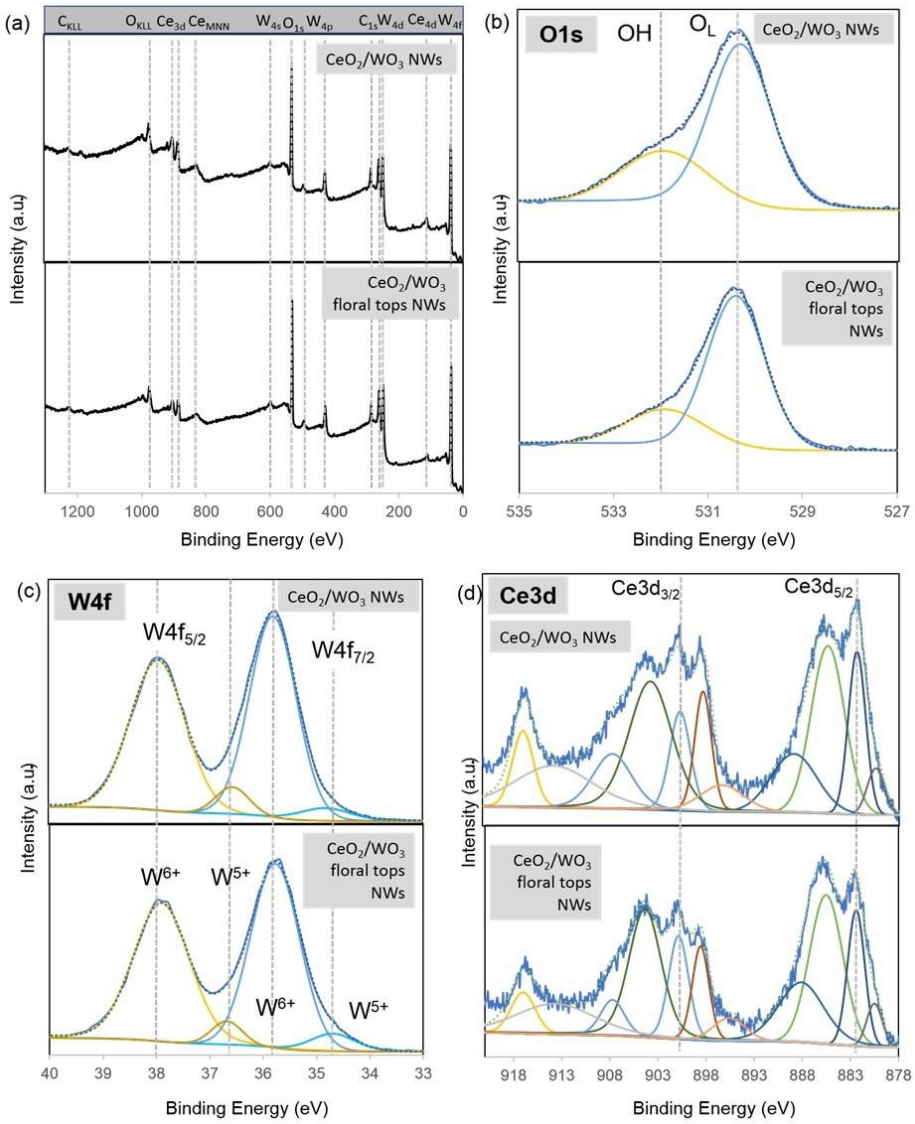

Figure 1: XPS spectra of the CeO_2/WO_3 floral tops NWs and the CeO_2/WO_3 NWs (a) full spectra, (b) O1s, (c) W4f and (d) Ce3d BE.

Raman spectra of as prepared samples is presented in Figure 5. The spectrum indicates that all the samples have similar spectra. As can be seen from the Raman spectrum, three main regions appear at 600-900, 200-400 and below 200 cm^{-1} for WO_3 vibrations. The regions respectively correspond to stretching, deformation and lattice modes [40]. The WO_3 nanowire films exhibited well-defined Raman bands at 272, 326, 715 and 805 cm^{-1}. These bands are characteristic of the four intense vibrational modes of monoclinic WO_3 [41] confirming the XRD results that the WO_3 deposited by AACVD belongs to monoclinic phases. Also, the peak at 133 cm^{-1} is attributed to the relative translational or rotational motions of WO_6 octahedral units in the same unit cell (lattice models) [42]. The intense bands at 272 and 326 cm^{-1} are due to the bending modes of the bridging oxygen (W-O-W), whereas the bands at 715

and 805 cm^{-1} are assigned to the stretching modes (W + 6-O) [41]. There are no visible peaks directly corresponding to CeO_2 which is because of the low quantity of the CeO_2.

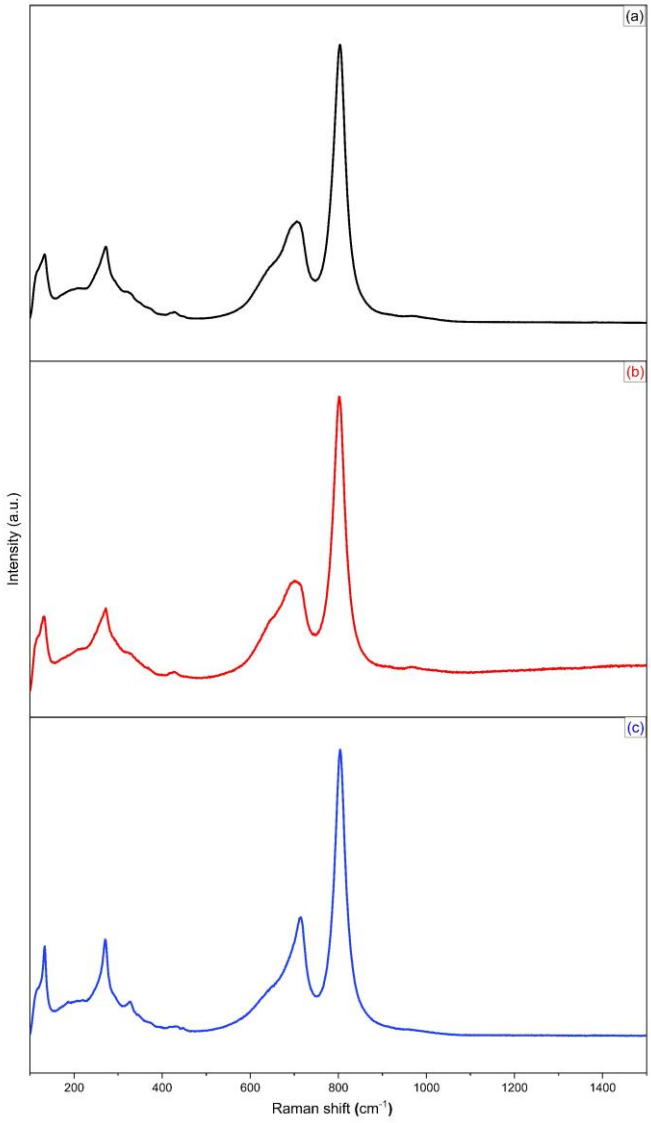

Figure 2: Raman spectra, (a) WO_3, (b) randomly oriented CeO_2 decorated WO_3 nanowires and (c) CeO_2 decorated WO_3 nanowires with floral tops.

3.2. Gas sensing response analysis.

Gas sensing tests were carried out at different concentrations of ethanol by using direct-current resistance measurements. The gas sensing characteristics of pristine and CeO_2 decorated WO_3 sensors towards oxidising gas (NO_2) as well as reducing gases (CO, ethanol, H_2) has been analysed and the sensor responses are calculated for oxidising gases as $R = \frac{R_{gas}}{R_{air}}$ and $R = \frac{R_{air}}{R_{gas}}$ for reducing gases. Pristine and CeO_2-decorated WO_3 nanowires were tested at temperatures ranging from room temperature up to

250ºC in order to understand the effect of the temperature on the sensor responses. More than three replicates of the measurements were performed to assess the reproducibility of the results. Figure 6**Error! No s'ha trobat l'origen de la referència. Error! No s'ha trobat l'origen de la referència.**displays the response of the different sensors tested towards 20 ppm of ethanol as a function of the operating temperature. None of the sensors responded to any concentrations of ethanol when operated below 100ºC, especially at RT or at 50ºC. Also, the response suddenly dropped beyond 250ºC and became unreproducible. This is because at too high temperatures the gas molecules start to desorb from the surface of the metal oxides[43]. Furthermore, at high temperatures, the oxidation of the surface of WO_3 proceeds faster than the reduction caused by the ethanol[44,45]. Therefore, 250ºC is the optimal working temperature for the pristine and CeO_2 decorated WO_3 nanowires and is adopted for all the investigations in case of ethanol sensing hereinafter.

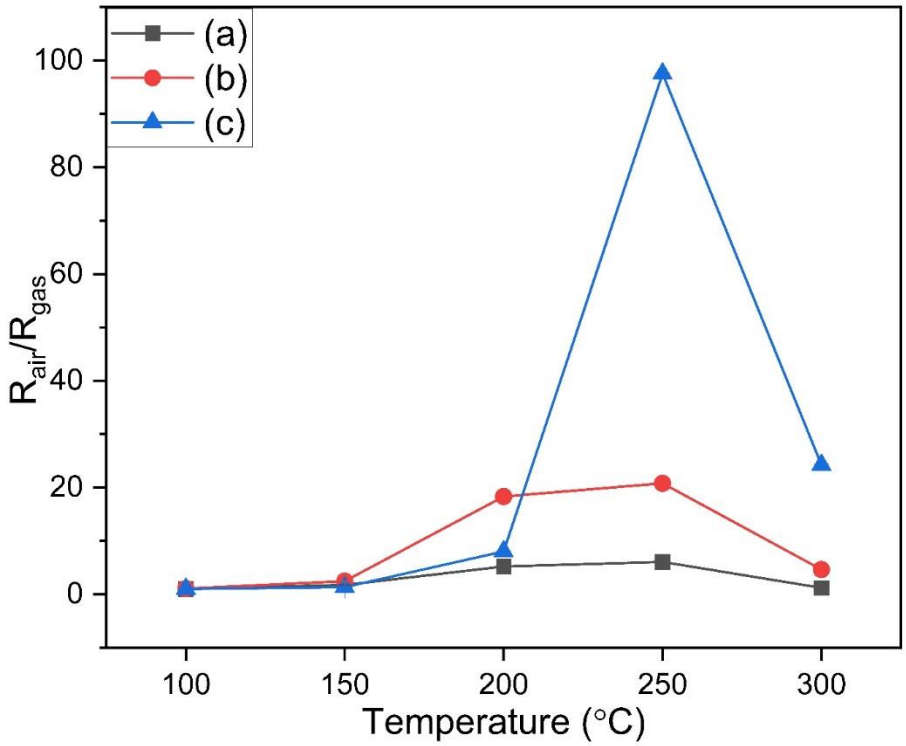

Figure 6: Sensor response to 20 ppm of ethanol as a function of operating temperature (a) WO_3, (b) randomly oriented CeO_2 decorated WO_3 nanowires and (c) CeO_2 decorated WO_3 nanowires with floral tops.

Figure 7illustrates the resistance changes of pristine and CeO_2 decorated WO_3 nanowires towards ethanol pulses with concentrations ranging from 5 to 20 ppm at the working optimum temperature

(250°C). When exposed to the reducing gas ethanol, the sensors displayed an n-type semiconducting behaviour, which is characterized by a decrease in the electrical resistance when exposed to ethanol vapours. The response of the sensors was stable as was demonstrated by full baseline resistance recovery. To check the reproducibility of the sensor responses, the sensors were re-exposed to 5 ppm of ethanol as is shown in Figure S4 (Supporting Information). The sensors showed reproducible behaviour. The corresponding gas-sensing responses calculated from the change in resistance of pristine WO_3 and CeO_2 decorated WO_3 nanowires are plotted as a function of the ethanol concentration as shown in Figure 8. The results of the pristine WO_3 are similar to the ones reported in our previous works[35]. As is evident from the results, the decoration of WO_3 nanowires with CeO_2 has greatly enhanced the sensitivity towards ethanol. At the lowest concentration of ethanol used (5 ppm), the response of CeO_2 decorated floral top WO_3 nanowires is 72 times higher than the pristine WO_3. The sensitivity of the pure WO_3 sensor towards ethanol was very small as compared to the CeO_2 decorated WO_3 sensors especially the ones with floral top nanowires. The sensor corresponding resistance changes towards the lowest concentration of ethanol (5ppm) at 250°C are shown in Figure S4. The variation of baseline resistance as a function of temperature in is shown in Figure S6.

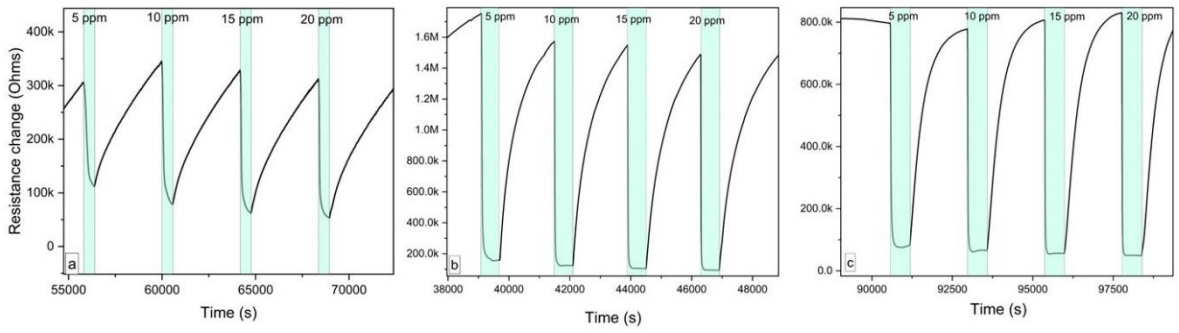

Figure 7: Film resistance changes (a) WO_3, (b) randomly oriented CeO_2 decorated WO_3 nanowires (c) CeO_2 decorated WO_3 nanowires with floral tops towards various ethanol concentrations at 250°C.

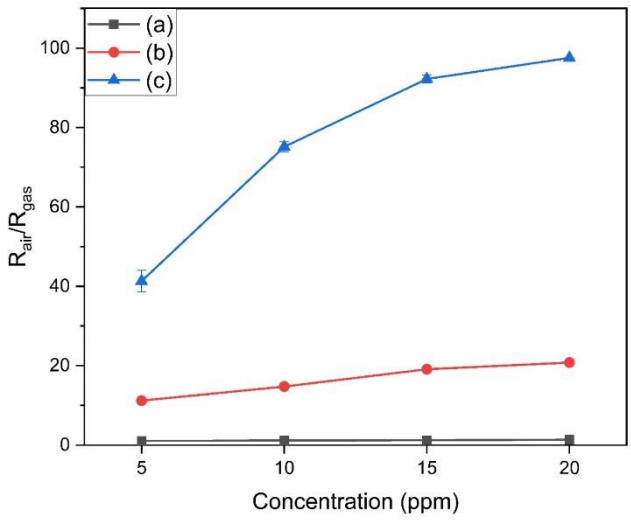

Figure 3: Sensor responses towards various ethanol concentrations at 250ºC (a) WO_3, (b) CeO_2 decorated WO_3 randomly oriented nanowires, and (c) CeO_2 decorated WO_3 nanowires with floral tops.

3.3. Nitrogen dioxide (NO_2)

The gas sensors were exposed towards different concentrations of NO_2 ranging from 100 ppb to 1 ppm. In our previous research[35], it was found that the response of WO_3 nanowires towards NO_2 decreases beyond 200ºC. We found the same trend in case of CeO_2 decorated WO_3 nanowires as well. Figure S7 (Supporting Information) shows the resistance change of the CeO_2 decorated WO_3 nanowires towards 500 ppb of NO_2 at 150ºC for pristine WO_3 and at 200ºC for CeO_2 decorated WO_3 nanowires. The response of the sensors towards various NO_2 concentrations is shown in Figure 9.

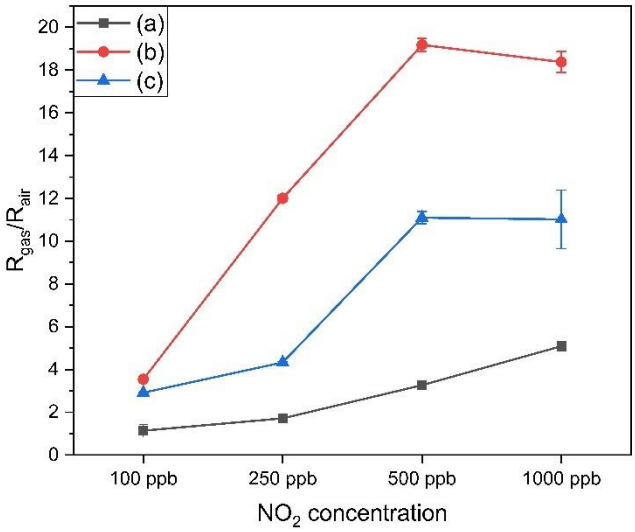

Figure 4: Sensor responses towards various NO_2 concentrations at 150°C (a) WO_3, and at 200°C for (b) CeO_2 decorated WO_3 randomly oriented nanowires, and (c) CeO_2 decorated WO_3 nanowires with floral tops.

Loading of tungsten trioxide with CeO_2 results in an increased responsiveness towards NO_2. In case of CeO_2 decorated WO_3, the maximum response was recorded at 200°C while as the response of pristine WO_3 is maximum at 150°C and starts to decrease with the increase of the temperature as is shown in Figure 10. The same trend was recorded in our previous research[36] for pristine WO_3 nanowires. Gas sensing results towards CO and H_2 are in presented in the supporting file.

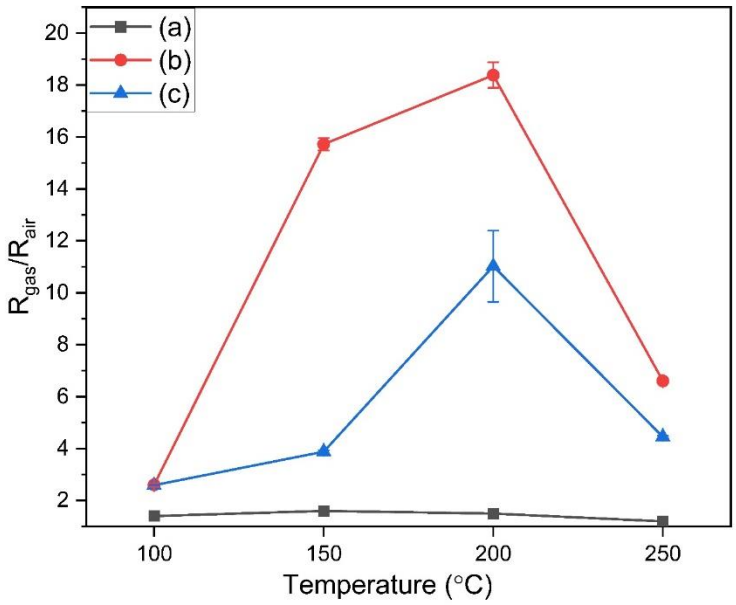

Figure 5: NO_2 sensing results for 1 ppm (a) WO_3, (b) CeO_2 decorated WO_3 randomly oriented nanowires, and (c) CeO_2 decorated WO_3 nanowires with floral tops.

Finally, the responses to CO and to H_2 were also studied. These results can be found in the Supporting Information (Figure S8 and S9 for CO and Figures S10 and S11 for H_2).

3.4. Selectivity test

Selectivity is an important parameter to be considered in gas detection, since it demonstrates the ability of the sensor to discriminate the target gas from interfering gases. Herein, we chose H_2, NO_2 and CO as interfering gases; their concentrations were equal or higher than that of ethanol, except for NO_2, where its concentration was 1 ppm, which is actually a high concentration (e.g., the EPA has set the annual average NO_2 standard of 53 ppb), OSHA PEL recommendations for CO (25 ppm) and NO_2 (1 ppm) for eight-hour average exposure. Figure 11 illustrates the obtained results. It is clear that incorporating CeO_2 in the WO_3 host matrix, enhances the responses towards ethanol especially in case of CeO_2 decorated WO_3 nanowires with floral tops. Indeed, at an operating temperature of 250ºC, the response of this sensor was 10-fold higher than that of pristine WO_3 and 5-fold higher than that of CeO_2 decorated WO_3 randomly oriented nanowires. Moreover, its responses towards the interfering gases, at the 250ºC, were negligible and very weak compared to the one of ethanol. Therefore, CeO_2 decorated WO_3 nanowires with floral tops exhibit excellent sensitivity and selectivity towards ethanol.

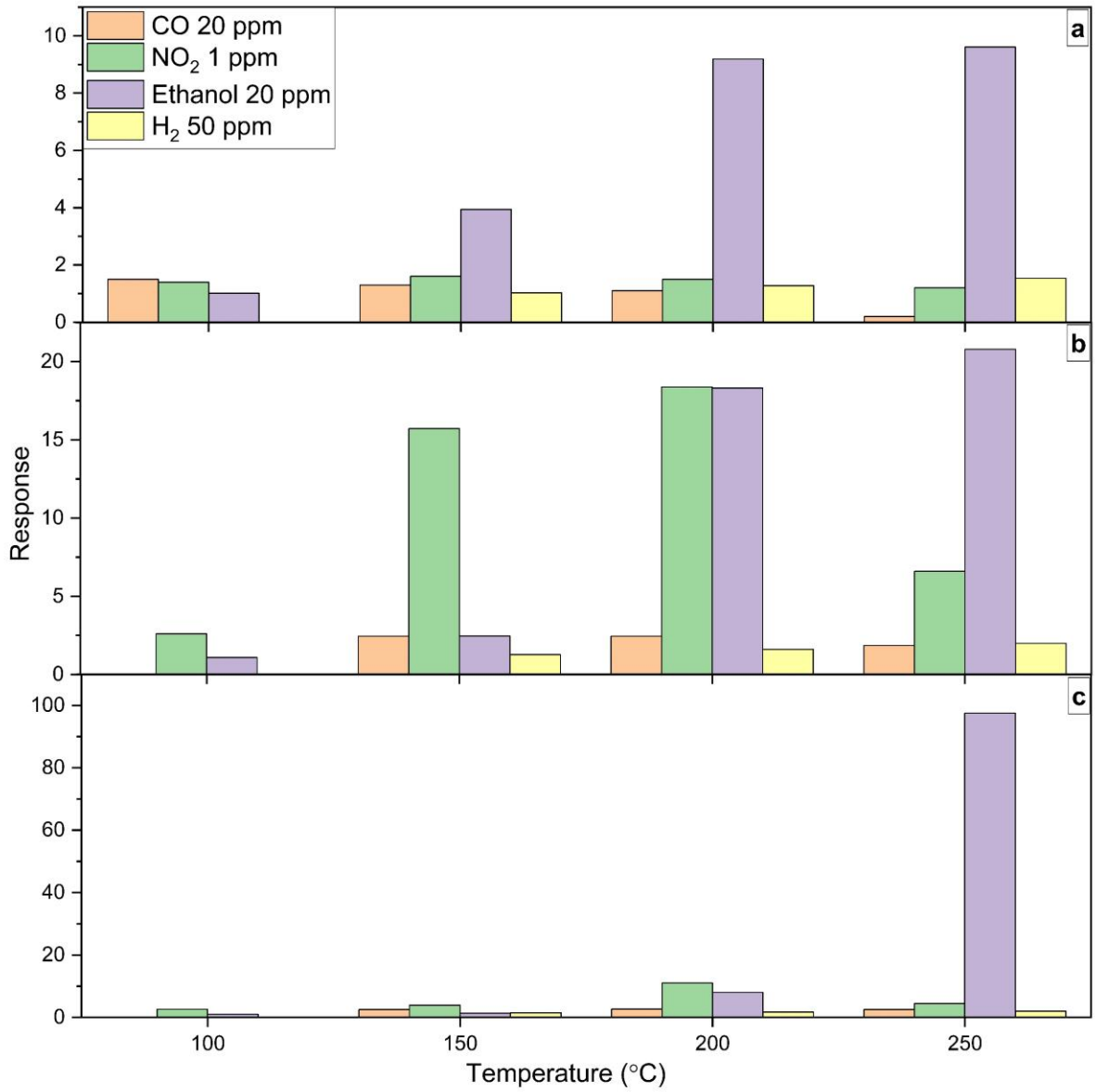

Figure 6: Selectivity histogram of (a) WO_3, (b) CeO_2 decorated WO_3 randomly oriented nanowires, and (c) CeO_2 decorated WO_3 nanowires with floral tops.

3.5. Humidity measurements

The impact of water vapour on the sensing performance is one of the most crucial aspects to consider while developing chemoresistive metal oxide gas sensors. The electrical properties and sensitivity of the metal oxide sensors is dramatically influenced by the presence of moisture. To study the effect of humidity on the sensor responses, the influence of 50 % relative humidity (RH) at RT on the sensor performance was also analysed. There is a 69 % decrease in the sensing response in case of pristine WO_3 nanowires, 73 % drop in the sensing response in case of CeO_2 decorated WO_3 floral nanowires

and 76 % decrease in case of CeO_2 decorated randomly oriented WO_3 nanowires under humid atmosphere. However, the baseline recovery in humid environment is more promising than in the dry conditions in case of CeO_2 decorated WO_3 nanowires as can be seen in Figure S12 (Supporting Information). There is comparatively less noise in the measured values under humid conditions than under dry conditions. The decrease in the response can be owed to the competition between the water molecules (formation of hydroxyl groups) and ethanol active sites[46]. Upon removal of the humidity, the sensors baseline resistances are recovered and so are the responses towards ethanol.

Table 1 summarizes the comparison of sensing properties of CeO_2 decorated WO_3 and previously published works. Compared to the majority of the works shown in the table, our sensors exhibit great sensitivity to the target gases at lower working temperatures. Also, our sensors can detect ethanol at low concentrations. Some studies do not report the humidity cross-sensitivity effects, despite ambient moisture significantly influences the electrical characteristics of gas sensors and impacts their sensitivity. Most reported results lack of data about the long-term stability of sensors. In our work, sensor responses have been gathered for more than 40 weeks, which has enabled assessing this aspect.

Structure	**Host Matrix**	**Nps[$]**	**T_{op} (^oC)**	**Conc. (ppm)**	**Response**	**Selectivity test**	**Humidity effect studied**	**Reference**
CeO_2-WO_3	WO_3	CeO_2	250	20	97.6	Yes	Yes	This work
CeO_2-ZnO	ZnO	CeO_2	310	100	90	Yes	No	[47]
CeO_2-TiO_2	TiO_2	CeO_2	270	500	3.5	Yes	No	[48]
CeO_2-$ZnSnO_3$	$ZnSnO_3$	CeO_2	200	100	219.2	No	Yes	[49]
MoS_2/CeO_2	MoS_2	CeO_2	RT	50	7.5	Yes	Yes	[50]
CeO_2/ZnO	ZnO	CeO_2	310	100	90	Yes	No	[51]
WO_3	WO_3	-	250	50	20.5*	Yes	Yes	[12]

WO_3	WO_3	-	320	100	7.6	Yes	No	[52]
$ Nps: nanoparticles, T_{op} = operating temperature, * R = $\frac{G_{gas}-G_{air}}{G_{air}}$								

Table 1: Comparison of ethanol gas sensing performance of various sensors based on WO_3 and/or CeO_2 reported in literature.

4. Gas sensing mechanism

The interaction of the gas molecules with the surface of tungsten oxide includes adsorption onto the surface, electronic charge transfer and reduction/oxidation processes [53,54]. The atmospheric molecular oxygen reacts with the oxygen vacancies in the film chemisorbing oxygen in the form of O_2^-, O^-, O^{2-} depending on the sensor operating temperature [55,56]. The reactions are depicted in equations 1, 2 and 3. The chemisorbed oxygen species on the metal oxide semiconductor surface generate extrinsic surface acceptor states immobilizing conduction band electrons leading to the formation of a depletion layer.

$$O_{2\,(gas)} + e^- \rightarrow O^-_{2\,(ads)}\ (80\,℃ - 150\,℃) \qquad \textit{Equation 1}$$

$$O^-_{2\,(ads)} + e^- \rightarrow 2O^-_{(ads)}\ (150\ ℃ - 260\ ℃), \qquad \textit{Equation 2}$$

$$O^-_{(ads)} + e^- \rightarrow O^{2-}_{(ads)}\ (300\ ℃ - 500\ ℃) \qquad \textit{Equation 3}$$

When ethanol vapours interact, these chemisorbed oxygen species are consumed and electrons are released back to the conduction band of the *n*-type semiconductor. This leads to the decrease in the resistance of the sensing layers in the presence of ethanol and is illustrated by equation 4.

$$C_2H_5OH + 6O^- \rightarrow 2CO_2 + 3H_2O + 6e^- \qquad \text{Equation 4}$$

There is a possibility for the formation of intermediate reaction products like ethylene and water [57,58] due to the dehydration of WO_3 [12] as described in equation 5.

$$C_2H_5OH \rightarrow C_2H_4 + H_2O \qquad \text{Equation 5}$$

When WO_3 is decorated with CeO_2, electrons are transferred via the conduction band of WO_3 towards the CeO_2 nanoparticles, which are rich in oxygen vacancies [59]. Upon being exposed to synthetic air, oxygen molecules adsorb onto the active sites of the CeO_2 decorated WO_3. This leads to the extraction of electrons from the nanowire conduction band, leading to the formation of O^- species as dictated by the operating temperature (250ºC). An electron depletion layer is generated on the nanowires reducing the conduction band channel and increasing the resistance of the sensors. CeO_2 is known to possess high-mobility bulk oxygen vacancies, contributing to increasing the number of ionosorbed oxygen species at its surface, thus trapping electrons injected via the conduction band of the WO_3. Additionally, due to the small size of the CeO_2 nanoparticles (average size 3 nm), adsorbed oxygen species can spill-over at the CeO_2-WO_3 interface, resulting in more chemisorbed oxygen species on the surface of tungsten oxide nanowires [29]. This leads to an increase in the baseline resistance of the sensitive film, and also to a significant increase in the number of reactive sites. Again, exposure to ethanol vapours results in the consumption of surface oxygen species and release of initially trapped electrons towards the conduction bands of WO_3 and CeO_2. The power-law response analysis reported in the Supporting Information (Figure S5 and associated discussion) indicates that ethanol reacting with O^- would be responsible for the electrical response observed. Since the work function of WO_3 (4.8 eV) surpasses that of CeO_2 (4.69 eV) [33], the electrons released in CeO_2 resulting from the exposure to ethanol vapours are effectively injected towards WO_3 nanowires, thus contributing to the enhanced response observed in CeO_2-WO_3 hybrids compared to pristine WO_3 nanowires. The changes at the CeO_2-WO_3 heterojunction interface upon exposure to ethanol are illustrated in Figure 12.

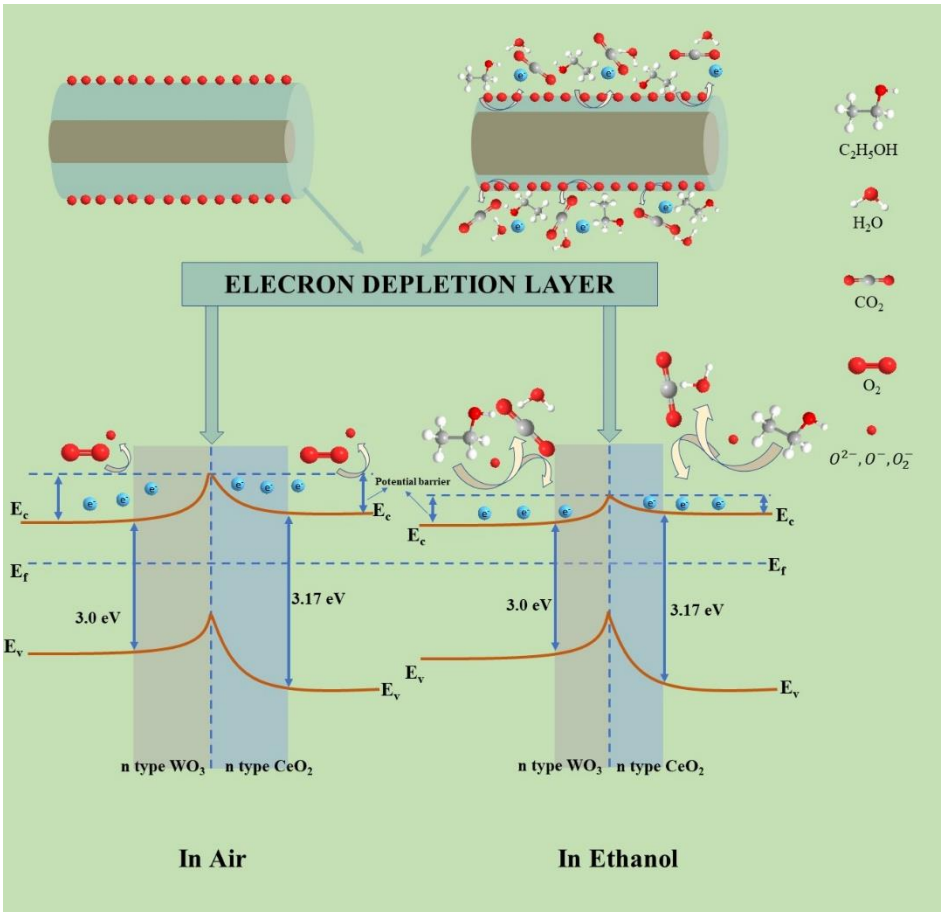

Figure 7: Proposed sensing mechanism of ethanol detection by CeO_2 decorated WO_3 nanowires.

Finally, the reason for the superior selectivity achieved for ethanol in comparison to other reducing species such as CO or H_2 may be due to the operating temperature selected that optimises the adsorption and reaction of ethanol and not of CO or H_2. Also, WO_3 is known for not being very reactive to CO [60].

5. Stability results

The sensor responses were checked over a period of 40 weeks. During this period sensors were regularly exposed to ethanol and to changing humidity backgrounds. Figure S shows the long-term stability of responses towards 5 ppm ethanol at 250°C. There is a 47.28 % decrease in the response from week 1 to week 19 in case of pristine WO_3 nanowires. This decrease is 56.04 % and 57.69 % for CeO_2 decorated WO_3 nanowires with floral tops and for randomly oriented CeO_2 decorated WO_3 nanowires, respectively. However, from week 19 to week 40, the responses of CeO_2 decorated WO_3 clearly stabilize, which is not the case for pristine WO_3. The sensors were not subjected to any sort of ageing

prior to starting the gas sensing measurements. Also, the sensors were exposed towards different gas species for selectivity tests. We perceive that the decrease in the sensor response from week 1 to week 19 is due to the ageing of the surface and around week 19 the surface is already aged and hence shows stable responses. The evolution of the baseline resistance can be found in the Supporting Information (Figure S13).

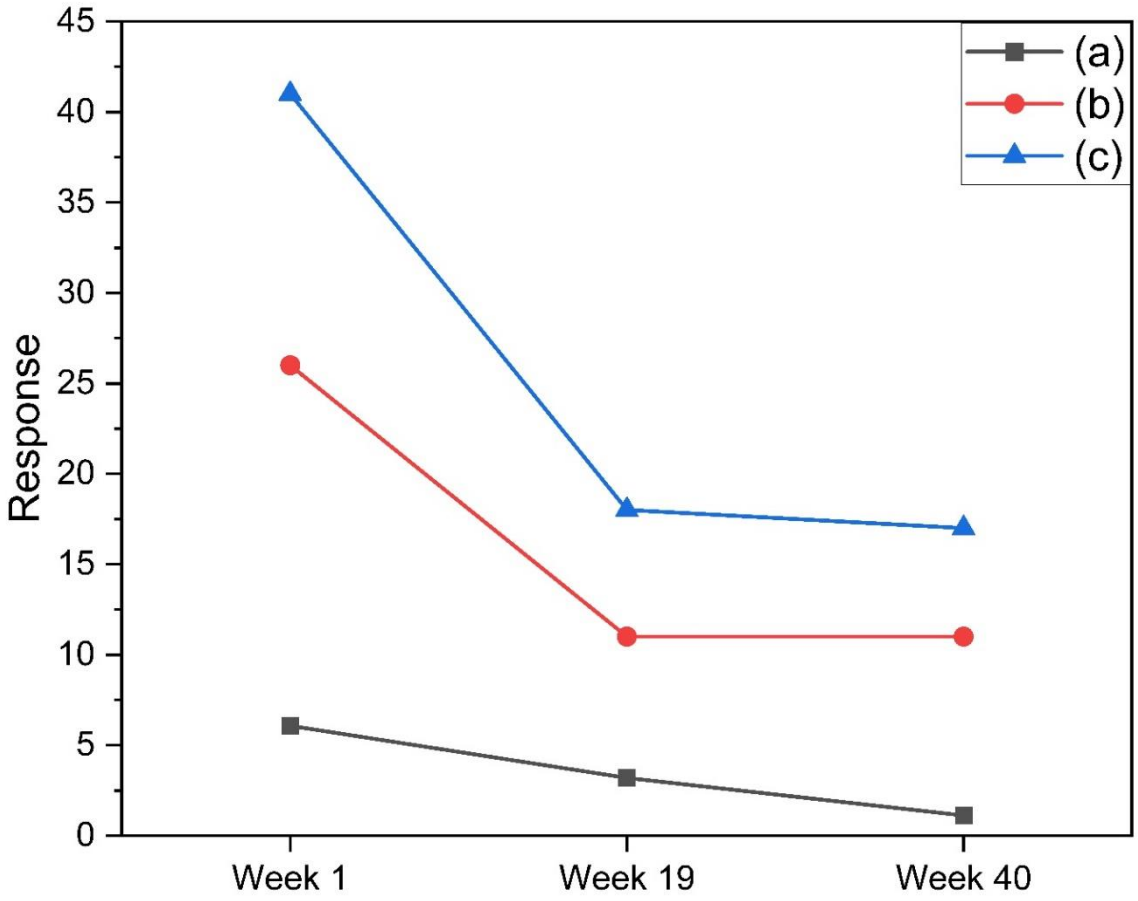

Figure 8: Long term stability study for the responses (a) WO_3, (b) CeO_2 decorated WO_3 randomly oriented nanowires, and (c) CeO_2 decorated WO_3 nanowires with floral tops towards 5 ppm ethanol at 250°C.

6. Conclusions

WO_3 nanowires have been successfully deposited onto alumina substrates by a one-step AACVD method. CeO_2 decorated WO_3 makes a desired heterojunction which demonstrates an effective route to bring functionality to WO_3. Pristine and CeO_2 decorated WO_3 nanowires show high purity and

crystallinity, as determined by XRD, FESEM and Raman techniques. The gas sensing experiments showed that the optimum working temperature is lower than in most metal oxide-based gas sensors. The sensors produced and studied show highly repeatable results with good long-term stability. CeO_2 decorated WO_3 nanowires show excellent sensitivity and fair selectivity towards ethanol vapours when operated at 250ºC. The superior sensitivity is attributed to hybrid nanomaterials having an increased concentration of oxygen surface species and, thus, higher number of reactive sites. These results clearly show the impact of decorating the WO_3 nanowires with CeO_2 for detecting ethanol.

Acknowledgements

This research is funded in part by MICINN grant no. TED2021-131442B-C31, and by AGAUR grant no. 2021 SGR 147. Shuja Bashir Malik is supported by Martí-Franquès Research grants Programme, Doctoral grants – 2019, (2019PMF-PIPF-14). E. Llobet is supported by the Catalan Institution for Research and Advanced Studies via the 2018 Edition of the ICREA Academia Award.

References

[1] A. Paleczek, D. Grochala, K. Staszek, S. Gruszczynski, E. Maciak, Z. Opilski, P. Kałużyński, M. Wójcikowski, T.V. Cao, A. Rydosz, An NO2 sensor based on WO3 thin films for automotive applications in the microwave frequency range, Sensors Actuators B Chem. 376 (2023). https://doi.org/10.1016/j.snb.2022.132964.

[2] Y. Zhang, L. Zhu, C. Qin, Y. Wang, J. Cao, Bimetal PtPd functionalized Bi2MoO6 microspheres for conductometric detection of CO: A combined experimental and theoretical study, Sensors Actuators B Chem. 381 (2023). https://doi.org/10.1016/j.snb.2023.133461.

[3] J.J. Rose, L. Wang, Q. Xu, C.F. McTiernan, S. Shiva, J. Tejero, M.T. Gladwin, Carbon monoxide poisoning: Pathogenesis, management, and future directions of therapy, Am. J. Respir. Crit. Care Med. 195 (2017) 596–606. https://doi.org/10.1164/rccm.201606-1275CI.

[4] M.J. Ahemad, T.D. Le, D.S. Kim, Y.T. Yu, Bimetallic AgAualloy@ZnO core-shell nanoparticles for ultra-high detection of ethanol: Potential impact of alloy composition on sensing performance, Sensors Actuators B Chem. 359 (2022) 131595. https://doi.org/10.1016/J.SNB.2022.131595.

[5] V. Postica, A. Vahl, D. Santos-Carballal, T. Dankwort, L. Kienle, M. Hoppe, A. Cadi-Essadek, N.H. De Leeuw, M.I. Terasa, R. Adelung, F. Faupel, O. Lupan, Tuning ZnO Sensors Reactivity toward Volatile Organic Compounds via Ag Doping and Nanoparticle Functionalization, ACS Appl. Mater. Interfaces. 11 (2019) 31452–31466. https://doi.org/10.1021/acsami.9b07275.

[6] S. Liu, W. Zeng, Y. Li, Synthesis of spherical WO3·H2O network for ethanol sensing application, Mater. Lett. 253 (2019) 42–45. https://doi.org/10.1016/J.MATLET.2019.06.037.

[7] C.S. Reddy, G. Murali, A.S. Reddy, S. Park, I. In, GO incorporated SnO2 nanotubes as fast response sensors for ethanol vapor in different atmospheres, J. Alloys Compd. 813 (2020) 152251. https://doi.org/10.1016/J.JALLCOM.2019.152251.

[8] Y. Wang, C. Liu, L. Wang, J. Liu, B. Zhang, Y. Gao, P. Sun, Y. Sun, T. Zhang, G. Lu, Horseshoe-shaped SnO2 with annulus-like mesoporous for ethanol gas sensing application, Sensors Actuators B Chem. 240 (2017) 1321–1329. https://doi.org/10.1016/J.SNB.2016.07.160.

[9] Q. Li, D. Chen, J. Miao, S. Lin, Z. Yu, D. Cui, Z. Yang, X. Chen, Highly sensitive sensor based on ordered porous ZnO nanosheets for ethanol detecting application, Sensors Actuators B Chem. 326 (2021) 128952. https://doi.org/10.1016/J.SNB.2020.128952.

[10] A. Alagh, F.E. Annanouch, K. Al Youssef, C. Bittencourt, F. Güell, P.R. Martínez-Alanis, M. Reguant, E. Llobet, PdO and PtO loaded WS2 boosts NO2 gas sensing characteristics at room temperature, Sensors Actuators B Chem. 364 (2022). https://doi.org/10.1016/j.snb.2022.131905.

[11] G. Neri, First fifty years of chemoresistive gas sensors, Chemosensors. 3 (2015) 1–20. https://doi.org/10.3390/chemosensors3010001.

[12] E. Spagnoli, S. Krik, B. Fabbri, M. Valt, M. Ardit, A. Gaiardo, L. Vanzetti, M. Della Ciana, V. Cristino, G. Vola, S. Caramori, C. Malagù, V. Guidi, Development and characterization of WO3 nanoflakes for selective ethanol sensing, Sensors Actuators B Chem. 347 (2021). https://doi.org/10.1016/j.snb.2021.130593.

[13] X. Wang, Y. Gao, Q. Zhang, X. He, X. Wang, Synthesis of MoO3 (1D) @SnO2 (2D) core-shell heterostructures for enhanced ethanol gas sensing performance, Sensors Actuators B Chem. 382 (2023) 133484. https://doi.org/10.1016/J.SNB.2023.133484.

[14] F. Liu, G. Huang, X. Wang, X. Xie, G. Xu, G. Lu, X. He, J. Tian, H. Cui, High response and selectivity of single crystalline ZnO nanorods modified by In2O3 nanoparticles for n-butanol gas sensing, Sensors Actuators B Chem. 277 (2018) 144–151. https://doi.org/10.1016/J.SNB.2018.08.144.

[15] X. Wang, F. Liu, X. Chen, X. Song, G. Xu, Y. Han, J. Tian, H. Cui, In2O3 Nanoparticles Decorated ZnO Hierarchical Structures for n-Butanol Sensor, ACS Appl. Nano Mater. 3 (2020) 3295–3304. https://doi.org/10.1021/acsanm.0c00025.

[16] K. Wang, W. Wei, Z. Lou, H. Zhang, L. Wang, 1D/2D heterostructure nanofiber flexible sensing device with efficient gas detectivity, Appl. Surf. Sci. 479 (2019) 209–215. https://doi.org/10.1016/J.APSUSC.2019.02.094.

[17] S. Wang, X. Wang, G. Qiao, X. Chen, X. Wang, H. Cui, Core-double shell ZnO@In2O3@ZnO hollow microspheres for superior ethanol gas sensing, Sensors Actuators B Chem. 341 (2021) 130002. https://doi.org/10.1016/J.SNB.2021.130002.

[18] H. Wang, Z. Feng, Y. Zhang, D. Han, J. Ma, X. Chai, S. Sang, Highly sensitive and low detection limit NO2 gas sensor based on In2O3 nanoparticles modified peach kernel-like GaN composites, Sensors Actuators B Chem. 382 (2023) 133452. https://doi.org/10.1016/J.SNB.2023.133452.

[19] Q. Zhang, Q. Ma, X. Wang, Y. Wang, D. Zhao, Surface Double Oxygen Defect Engineering in Button-Shaped Porous Ceo2/Wo2.9 Heterostructures for Excellent N-Butanol Detection at Room Temperature, SSRN Electron. J. 616 (2022). https://doi.org/10.2139/ssrn.4296261.

[20] P. Hu, J. Chen, Q. Ma, J. Yin, D. Zhou, C. Kou, J. Xu, J. Xu, One-step thermal compensation decomposition synthesis of ZnWO4/WO3 composite with synergy of multiple structural effects for efficient trace H2S detection, Sensors Actuators B Chem. 381 (2023) 133388. https://doi.org/10.1016/J.SNB.2023.133388.

[21] J. Zhang, D. Leng, G. Li, J. Liu, H. Wang, Y. Zhu, H. Lu, J. Gao, B. Zhu, Bimetallic–organic framework-derived Co3O4–ZnO heterojunction nanofibers: A new kind of emerging porous nanomaterial for enhanced ethanol sensing, Sensors Actuators B Chem. 349 (2021). https://doi.org/10.1016/j.snb.2021.130732.

[22] G. Li, Y. Zhang, Q. Liang, J. Zhang, J. Liu, Y. Liu, C. Wang, J. Gao, H. Lu, Nanoporous Co3O4–TiO2 Heterojunction Nanosheets for Ethanol Sensing, ACS Appl. Nano Mater. 5 (2022) 4779–4786. https://doi.org/10.1021/acsanm.1c04259.

[23] T.L.H. Doan, J.Y. Kim, J.H. Lee, L.H.T. Nguyen, Y.T. Dang, K.B.T. Bui, A.T.T. Pham, A. Mirzaei, T.B. Phan, S.S. Kim, Preparation of n-ZnO/p-Co3O4 heterojunctions from zeolitic imidazolate frameworks (ZIF-8/ZIF-67) for sensing low ethanol concentrations, Sensors Actuators B Chem. 348 (2021). https://doi.org/10.1016/j.snb.2021.130684.

[24] J. Fang, X. Chen, R.P. Xiao, J.J. Xue, J.M. Song, High performance ethanol sensor based on Pr-SnO2/In2O3 composite, Ceram. Int. 48 (2022) 9897–9905. https://doi.org/10.1016/j.ceramint.2021.12.193.

[25] H. Cao, Z. Hu, X. Wei, H. Wang, X. Tian, S. Ding, Conductometric ethanol gas sensor based on a bilayer film consisting of SnO2 film and SnO2/ZnSnO3 porous film prepared by magnetron sputtering, Sensors Actuators B Chem. 382 (2023). https://doi.org/10.1016/j.snb.2023.133562.

[26] P. Wang, S.Z. Wang, Y.R. Kang, Z. Sen Sun, X.D. Wang, Y. Meng, M.H. Hong, W.F. Xie, Cauliflower-shaped Bi2O3–ZnO heterojunction with superior sensing performance towards ethanol, J. Alloys Compd. 854 (2021) 157152. https://doi.org/10.1016/J.JALLCOM.2020.157152.

[27] H. Li, Z. Yang, W. Ling, D. Zhu, Y. Pu, UV excited gas sensing SnO2-ZnO aerogels to ppb-level ethanol detection, Sensors Actuators, B Chem. 337 (2021). https://doi.org/10.1016/j.snb.2021.129815.

[28] S. Agarwal, P. Rai, E.N. Gatell, E. Llobet, F. Güell, M. Kumar, K. Awasthi, Gas sensing properties of ZnO nanostructures (flowers/rods)synthesized by hydrothermal method, Sensors Actuators, B Chem. 292 (2019) 24–31. https://doi.org/10.1016/j.snb.2019.04.083.

[29] K. Yuan, C.Y. Wang, L.Y. Zhu, Q. Cao, J.H. Yang, X.X. Li, W. Huang, Y.Y. Wang, H.L. Lu, D.W. Zhang, Fabrication of a Micro-Electromechanical System-Based Acetone Gas Sensor Using CeO2 Nanodot-Decorated WO3 Nanowires, ACS Appl. Mater. Interfaces. 12 (2020) 14095–14104. https://doi.org/10.1021/acsami.9b18863.

[30] F. Pourfayaz, A. Khodadadi, Y. Mortazavi, S.S. Mohajerzadeh, CeO2 doped SnO2 sensor selective to ethanol in presence of CO, LPG and CH4, Sensors Actuators, B Chem. 108 (2005) 172–176. https://doi.org/10.1016/j.snb.2004.12.107.

[31] L. Lei, Y. Wang, Z. Zhang, J. An, F. Wang, Transformations of Biomass, Its Derivatives, and Downstream Chemicals over Ceria Catalysts, ACS Catal. 10 (2020) 8788–8814. https://doi.org/10.1021/acscatal.0c01900.

[32] Z. Dong, Q. Hu, H. Liu, Y. Wu, Z. Ma, Y. Fan, R. Li, J. Xu, X. Wang, 3D flower-like Ni doped CeO2 based gas sensor for H2S detection and its sensitive mechanism, Sensors Actuators B Chem. 357 (2022) 131227. https://doi.org/10.1016/J.SNB.2021.131227.

[33] J. Liu, M. Dai, T. Wang, P. Sun, X. Liang, G. Lu, K. Shimanoe, N. Yamazoe, Enhanced Gas Sensing Properties of SnO2 Hollow Spheres Decorated with CeO2 Nanoparticles Heterostructure Composite Materials, ACS Appl. Mater. Interfaces. 8 (2016) 6669–6677. https://doi.org/10.1021/acsami.6b00169.

[34] È. Navarrete, C. Bittencourt, X. Noirfalise, P. Umek, E. González, F. Güell, E. Llobet, WO3 nanowires loaded with cobalt oxide nanoparticles, deposited by a two-step AACVD for gas sensing applications, Sensors Actuators, B Chem. 298 (2019) 126868. https://doi.org/10.1016/j.snb.2019.126868.

[35] E. Navarrete, C. Bittencourt, P. Umek, E. Llobet, AACVD and gas sensing properties of nickel oxide nanoparticle decorated tungsten oxide nanowires, J. Mater. Chem. C. 6 (2018) 5181–5192.

https://doi.org/10.1039/c8tc00571k.

[36] E. Navarrete, C. Bittencourt, P. Umek, D. Cossement, F. Güell, E. Llobet, Tungsten trioxide nanowires decorated with iridium oxide nanoparticles as gas sensing material, J. Alloys Compd. 812 (2020). https://doi.org/10.1016/j.jallcom.2019.152156.

[37] T. Berestok, P. Guardia, J. Blanco, R. Nafria, P. Torruella, L. López-Conesa, S. Estradé, M. Ibáñez, J. De Roo, Z. Luo, D. Cadavid, J.C. Martins, M. V. Kovalenko, F. Peiró, A. Cabot, Tuning Branching in Ceria Nanocrystals, Chem. Mater. 29 (2017) 4418–4424. https://doi.org/10.1021/acs.chemmater.7b00896.

[38] F.E. Annanouch, Z. Haddi, M. Ling, F. Di Maggio, S. Vallejos, T. Vilic, Y. Zhu, T. Shujah, P. Umek, C. Bittencourt, C. Blackman, E. Llobet, Aerosol-Assisted CVD-Grown PdO Nanoparticle-Decorated Tungsten Oxide Nanoneedles Extremely Sensitive and Selective to Hydrogen, ACS Appl. Mater. Interfaces. 8 (2016). https://doi.org/10.1021/acsami.6b00773.

[39] F. Güell, P.R. Martínez-Alanis, S. Roso, C.I. Salas-Pérez, M.F. García-Sánchez, G. Santana, B.M. Monroy, Plasma versus thermal annealing for the Au-catalyst growth of ZnO nanocones and nanowires on Al-doped ZnO buffer layers, Mater. Res. Express. 3 (2016) 1–11. https://doi.org/10.1088/2053-1591/3/6/065013.

[40] M.F. Daniel, B. Desbat, J.C. Lassegues, B. Gerand, M. Figlarz, Infrared and Raman study of WO3 tungsten trioxides and WO3, xH2O tungsten trioxide tydrates, J. Solid State Chem. 67 (1987) 235–247. https://doi.org/10.1016/0022-4596(87)90359-8.

[41] T. Nishide, F. Mizukami, Crystal structures and optical properties of tungsten oxide films prepared by a complexing-agent-assisted sol-gel process, Thin Solid Films. 259 (1995) 212–217. https://doi.org/10.1016/0040-6090(94)06444-X.

[42] L. Pirker, B. Višić, J. Kovač, S.D. Škapin, M. Remškar, Synthesis and characterization of tungsten suboxide wn o3n−1 nanotiles, Nanomaterials. 11 (2021) 1–12. https://doi.org/10.3390/nano11081985.

[43] D. Wei, Z. Huang, L. Wang, X. Chuai, S. Zhang, G. Lu, Hydrothermal synthesis of Ce-doped hierarchical flower-like In2O3 microspheres and their excellent gas-sensing properties, Sensors Actuators B Chem. 255 (2018) 1211–1219. https://doi.org/10.1016/J.SNB.2017.07.162.

[44] D.J. Dwyer, Surface chemistry of gas sensors: H2S on WO3 films, Sensors Actuators B Chem. 5 (1991) 155–159. https://doi.org/10.1016/0925-4005(91)80237-E.

[45] Q. Diao, Y. Yin, W. Jia, X. Xu, Y. Ding, X. Zhang, J. Cao, K. Yang, M. Jiao, Highly sensitive ethanol sensor based on Ce-doped WO3with raspberry-like architecture, Mater. Res. Express. 7 (2020). https://doi.org/10.1088/2053-1591/abcabf.

[46] F.E. Annanouch, Z. Haddi, S. Vallejos, P. Umek, P. Guttmann, C. Bittencourt, E. Llobet, Aerosol-assisted CVD-grown WO3 nanoneedles decorated with copper oxide nanoparticles for the selective and humidity-resilient detection of H2S, ACS Appl. Mater. Interfaces. 7 (2015) 6842–6851. https://doi.org/10.1021/acsami.5b00411.

[47] G. Hui, M. Zhu, X. Yang, J. Liu, G. Pan, Z. Wang, Highly sensitive ethanol gas sensor based on CeO2/ZnO binary heterojunction composite, Mater. Lett. 278 (2020) 128453. https://doi.org/10.1016/J.MATLET.2020.128453.

[48] Y.J. Chen, G. Xiao, T.S. Wang, F. Zhang, Y. Ma, P. Gao, C.L. Zhu, E. Zhang, Z. Xu, Q.H. Li, Synthesis and enhanced gas sensing properties of crystalline CeO2/TiO2 core/shell nanorods, Sensors Actuators B Chem. 156 (2011) 867–874. https://doi.org/10.1016/J.SNB.2011.02.057.

[49] S. Yu, X. Jia, J. Yang, S. Wang, Y. Li, H. Song, Highly sensitive and low detection limit of ethanol gas sensor based on CeO2 nanodot-decorated ZnSnO3 hollow microspheres, Ceram. Int. 48 (2022) 14865–14875. https://doi.org/10.1016/J.CERAMINT.2022.02.023.

[50] J. Zhang, T. Li, J. Guo, Y. Hu, D. Zhang, Two-step hydrothermal fabrication of CeO2-loaded MoS2 nanoflowers for ethanol gas sensing application, Appl. Surf. Sci. 568 (2021) 150942. https://doi.org/10.1016/J.APSUSC.2021.150942.

[51] G. Hui, M. Zhu, X. Yang, J. Liu, G. Pan, Z. Wang, Highly sensitive ethanol gas sensor based on CeO2/ZnO binary heterojunction composite, Mater. Lett. 278 (2020). https://doi.org/10.1016/j.matlet.2020.128453.

[52] J. Huang, X. Xu, C. Gu, M. Yang, M. Yang, J. Liu, Large-scale synthesis of hydrated tungsten oxide 3D architectures by a simple chemical solution route and their gas-sensing properties, J. Mater. Chem. 21 (2011) 13283–13289. https://doi.org/10.1039/c1jm11292a.

[53] M.F. Al-Kuhaili, S.M.A. Durrani, I.A. Bakhtiari, Carbon monoxide gas-sensing properties of CeO2-WO3 thin films, Mater. Sci. Technol. 26 (2010) 726–731. https://doi.org/10.1179/174328409X443209.

[54] B. Saruhan, R. Lontio Fomekong, S. Nahirniak, Review: Influences of Semiconductor Metal Oxide Properties on Gas Sensing Characteristics, Front. Sensors. 2 (2021) 1–24. https://doi.org/10.3389/fsens.2021.657931.

[55] N. Barsan, U. Weimar, Conduction model of metal oxide gas sensors, J. Electroceramics. 7 (2001) 143–167. https://doi.org/10.1023/A:1014405811371.

[56] S. Agarwal, P. Rai, E. Navarrete, E. Llobet, F. Güell, Sensors and Actuators B : Chemical Gas sensing properties of ZnO nanostructures (fl owers / rods) synthesized by hydrothermal method, 292 (2019) 24–31.

[57] Z. Tang, X. Deng, Y. Zhang, X. Guo, J. Yang, C. Zhu, J. Fan, Y. Shi, B. Qing, F. Fan, MoO3 nanoflakes coupled reduced graphene oxide with enhanced ethanol sensing performance and mechanism, Sensors Actuators B Chem. 297 (2019) 126730. https://doi.org/10.1016/j.snb.2019.126730.

[58] A.E.-A. A. Said, M.M.M.A. El-Wahab, M.A. El-Aal, The Role of Acid Sites in the Catalytic Performance of Tungsten Oxide during the Dehydration of Isopropyl and Methyl Alcohols, Chem. Mater. Eng. 4 (2016) 17–25. https://doi.org/10.13189/cme.2016.040202.

[59] S. Yu, X. Jia, J. Yang, S. Wang, Y. Li, H. Song, Highly sensitive and low detection limit of ethanol gas sensor based on CeO2 nanodot-decorated ZnSnO3 hollow microspheres, Ceram. Int. 48 (2022) 14865–14875. https://doi.org/10.1016/j.ceramint.2022.02.023.

[60] A. Staerz, S. Somacescu, M. Epifani, T. Kida, U. Weimar, and N. Barsan, “WO3-Based Gas Sensors: Identifying Inherent Qualities and Understanding the Sensing Mechanism,” ACS Sensors, vol. 5, no. 6, pp. 1624–1633, 2020, doi: 10.1021/acssensors.0c00113.